

GaussianHead: High-fidelity Head Avatars with Learnable Gaussian Derivation

Jie Wang¹, Jiu-Cheng Xie^{1*}, Xianyan Li¹, Feng Xu², Chi-Man Pun³, Hao Gao^{1*}

¹Nanjing University of Posts and Telecommunications

²Tsinghua University

³University of Macau

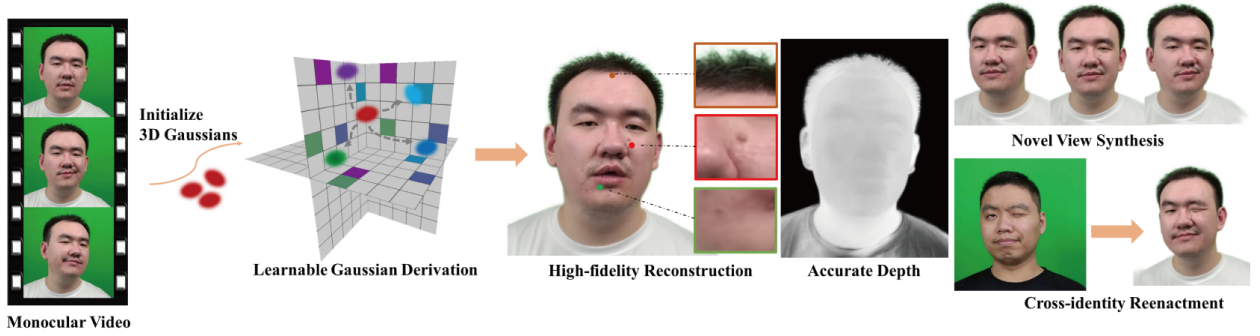


Figure 1: Based on anisotropic 3D Gaussians and the learnable derivation strategies, our method learns an identity-specific head avatar from a monocular video of the corresponding subject. The proposed GaussianHead demonstrates outstanding performance in self-reconstruction, novel-view synthesis and cross-identity reenactment tasks.

Abstract

Constructing vivid 3D head avatars for given subjects and realizing a series of animations on them is valuable yet challenging. This paper presents GaussianHead, which models the actional human head with anisotropic 3D Gaussians. In our framework, a motion deformation field and multi-resolution tri-plane are constructed respectively to deal with the head’s dynamic geometry and complex texture. Notably, we impose an exclusive derivation scheme on each Gaussian, which generates its multiple doppelgangers through a set of learnable parameters for position transformation. With this design, we can compactly and accurately encode the appearance information of Gaussians, even those fitting the head’s particular components with sophisticated structures. In addition, an inherited derivation strategy for newly added Gaussians is adopted to facilitate training acceleration. Extensive experiments show that our method can produce high-fidelity renderings, outperforming state-of-the-art approaches in reconstruction, cross-identity reenactment, and novel view synthesis tasks. Our code is available at <https://github.com/chiehwangsgaussian-head>.

1 Introduction

Creating personalized avatars for everyone is crucial in the future wide-ranging applications of virtual reality. Early methods mostly create surface templates for head avatars without details, based on face data obtained from extensive scans [Gerig *et al.*, 2018; Li *et al.*, 2017]. Building implicit head avatars using Signed Distance Fields (SDF) [Yariv *et al.*, 2020; Yariv *et al.*, 2021] helps overcome the deficiencies of skinned models and achieve better head geometry [Zheng *et al.*, 2022]. Nevertheless, implicit surfaces lack enough expressive power for fine structures and suffer from inefficient rendering. Combining explicit data structures and volume rendering to build volumetric neural radiance fields gradually becomes the current mainstream practice. Methods like [Gao *et al.*, 2022; Tang *et al.*, 2022; Li *et al.*, 2023; Xu *et al.*, 2023a] can generate visually impressive head avatars by encoding scenes using voxels or multiple 2D planes. Nevertheless, these approaches are constrained by the resolution restrictions associated with explicit structures and the drawbacks introduced by “feature dilution” resulting from axis-aligned mappings.

To be more specific, primitives on the same projection line (represented by the cyan, blue, and green blocks in Fig. 2) are repetitively mapped to the same position on the feature plane. Moreover, due to the finite resolution of the plane, primitives in close neighboring regions (the orange and red blocks in Fig. 2) are also projected on the same grid. These two conditions are collectively referred to as “feature dilu-

*Corresponding author.

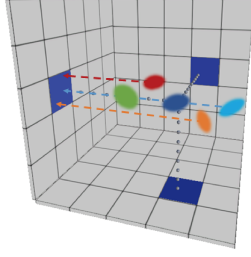


Figure 2: The adoption of axis-aligned mapping is accompanied by a severe problem of “feature dilution”, detailed explanations of that are given in the second paragraph of the Introduction part.

tion”. As a consequence, the features stored at a certain grid point are no longer exclusively connected to a specific primitive. It reduces the distinguishability among primitives, eventually weakening the representational capacity for sophisticated situations. Problems become more pronounced in particular head areas with complex geometry, such as regions obscured by lips, hair, and wrinkles, where denser primitives often exist, accompanied by a significant occurrence of overlapping. TILTED [Yi *et al.*, 2023] aims to achieve a more accurate feature representation of these primitives interpolated on the factor planes through simultaneous rotation of the entire scene. While it appears to be effective in static scenarios, shortcomings arise in dynamic scenes. The inherent dynamism of objects disrupts those attempts to address misalignments by relying on overall scene rotations. Additionally, it is less effective in mitigating specific feature dilution within overlapped structures.

In this paper, we introduce the GaussianHead, a new method based on deformable 3D Gaussians for faithful head avatar construction and animation. Notably, we disentangle the modeling of head geometry and texture attributes. To be concrete, a motion deformation field is first built to fit the whole head shape as well as dynamic facial movements. In practice, it takes pre-retrieved facial expression parameters as conditions to transform randomly initialized 3D Gaussians into a canonical space. Then we employ an explicit data container—parameterized multi-resolution tri-plane—to store the appearance information of those Gaussians. To resolve the aforementioned feature dilution issue, we design a novel Gaussian derivation strategy. In short, we generate multiple derivations of each core Gaussian in the canonical space using sets of learnable rotation transformations. By acquiring sub-features from these derived doppelgangers and integrating them, we are able to obtain the precise canonical features of the current Gaussian. Moreover, a mechanism of inheritance derivation initialization is adopted for newly added Gaussians in the later training phase, improving convergence speed.

Overall, our contributions are as follows:

- Leveraging anisotropic 3D Gaussian primitives and explicit parameterized tri-plane structures to construct dynamic head avatars enables high-fidelity results.
- The novel strategy of deriving core Gaussians addresses the feature dilution caused by axis-aligned mapping, re-

sulting in a more accurate representation of texture on complex structures.

- Extensive experiments on public datasets have shown that our method is superior to the latest alternatives in terms of visual effects and quantitative metrics.

2 Related Work

Scene Primitives in Reconstruction. Whether it is a real-world scenario, the human body, or a head, the foundation of their construction lies in a simple form of scene primitives. Some past approaches have relied on implicit primitives, such as the signed distance function [Yariv *et al.*, 2023; Yariv *et al.*, 2020; Park *et al.*, 2019] that builds objects by tracing points located on the zero-level set of the function in space or the occupancy function [Mescheder *et al.*, 2019; Zheng *et al.*, 2022; Peng *et al.*, 2020] that represents 3D surfaces as the continuous decision boundaries of deep neural network classifiers. However, these implicit primitives cannot represent complex head avatars. Neural radiance fields [Mildenhall *et al.*, 2021; Gafni *et al.*, 2021; Martin-Brualla *et al.*, 2021] store scenes using network weights, resulting in a significant training cost. Explicit scene primitives, such as points [Zheng *et al.*, 2023; Xu *et al.*, 2022], can capture sufficiently complex structures. However, due to the fixed shape of points, detailing can only be achieved by continuously refining point radii and increasing point counts during the training process, which introduces significant storage and training overhead. Here, we use 3D anisotropic Gaussians [Kerbl *et al.*, 2023] as scene primitives. They are deformable in geometric structure, allowing for the representation of intricate details by adjusting their shapes instead of blindly increasing quantity or reducing radii.

Monocular-video-based Head Portrait Synthesis. The widespread application of head avatars calls for convenient capture modes. Some studies [Cao *et al.*, 2021; Kirschstein *et al.*, 2023; Teotia *et al.*, 2023] utilize dense multi-view or binocular perspective to record dynamic head avatars in space. Although this brings better multi-view consistency, the difficulty of popularizing capture devices hinders the rapid adoption of such technologies. Meanwhile, they mostly reconstruct head dynamics along the temporal axis, sacrificing cross-subject generalization performance. Some portrait synthesis works start with a single image or a set of images, constructing identity-consistent head avatars through image-to-image transformations. [Zhang *et al.*, 2021; Yu *et al.*, 2023; Zhang *et al.*, 2023] use encoders to encode consistent identities from image sets and regulate outputs by fitting expressions or landmarks from 3D morphable model (3DMM). While achieving detailed rendered images, they lack multi-view consistency. Some head avatar methods utilizing monocular videos decouple appearance from the video [Hong *et al.*, 2022] or fit expressions and poses from it [Zheng *et al.*, 2022; Zheng *et al.*, 2023; Zielonka *et al.*, 2023; Gao *et al.*, 2022] as reconstruction conditions, achieving increasingly realistic results.

Hybrid Neural Field. Previous implicit methods, such as [Mildenhall *et al.*, 2021; Zheng *et al.*, 2022; Park *et al.*, 2019; Mescheder *et al.*, 2019] suggest that as the complexity of the scene increases, so does the network complexity and learn-

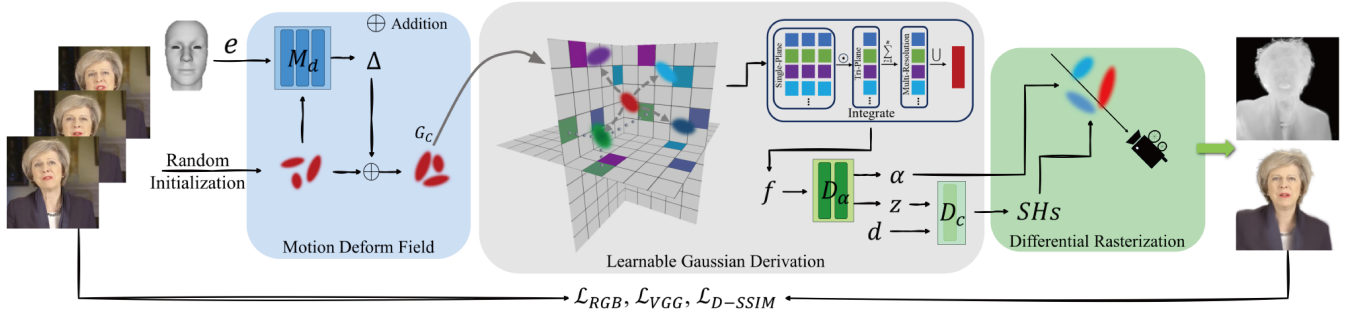


Figure 3: **Method overview.** GaussianHead uses a set of 3D Gaussians with learnable parameters controlling their shape and appearance to model the subject’s head. To represent the dynamic head geometry, a motion deformation field is first set up, which converts structureless Gaussians to structured core ones in a canonical space via conditioning on pre-acquired expression parameters e . A multi-resolution tri-plane is leveraged to store appearance-related attributes. Notably, derivation mechanisms through learnable rotations are applied to each core Gaussian G_c , yielding several doppelgangers of it. The integration of sub-features obtained through projection onto the planes from those doppelgangers is taken as the final canonical feature f of the core Gaussian. Two separate MLPs are employed to decode opacity α and spherical harmonic coefficients (SHs), based on which we generate the final rendering via differential rasterization. Notations \odot and \cup represent Hadamard product and concatenation operations, respectively.

ing difficulty. Recently, hybrid neural radiance fields have become a hot topic [Müller *et al.*, 2022; Xu *et al.*, 2023a; Gao *et al.*, 2022; Xu *et al.*, 2023b], storing scenes through explicit data structures (i.e., tri-plane [Chan *et al.*, 2022], hex-plane [Cao and Johnson, 2023; Fridovich-Keil *et al.*, 2023], voxel [Müller *et al.*, 2022]) to share the pressure of neural networks, allowing the latter to focus on decoding semantic information. However, the resolution limitations of explicit structures and the commonly employed axis-aligned mappings can lead to an imprecise representation of features. Our novel Gaussian derivation strategy successfully addresses the axis-aligned mapping limitations and brings excellent performance to complex regions.

3 Preliminary of 3D Gaussian Splatting

[Kerbl *et al.*, 2023] utilizes anisotropic 3D Gaussian primitives to explicitly represent the underlying structure of the scene. The structure of each Gaussian is determined by two parameters defined in world coordinates: position (mean) x and 3D covariance matrix Σ ,

$$G(x, \Sigma) = e^{-\frac{1}{2}x^T \Sigma^{-1}x}. \quad (1)$$

The intractable covariance matrix can be further decomposed into a scaling matrix S and a rotation matrix R , where the correlation between them is $\Sigma = RSS^T R^T$. For ease of optimization, we optimize a scaling vector s for S and a unit quaternion q for R in practice. Accordingly, the Gaussian is re-written as $G(x, q, s)$. In order to realize rendering, 3D Gaussians need to be projected onto the 2D image plane. Accordingly, the covariance matrix in camera coordinates can be obtained by $\Sigma' = JW\Sigma W^T J^T$, where W denotes the view transformation matrix and J represents the Jacobian matrix approximating the projective transformation [Zwicker *et al.*, 2002; Zwicker *et al.*, 2001]. On the other hand, the appearance of every Gaussian is affected by the other two parameters, namely the opacity α and spherical harmonic coefficients Y_{lm} , which are combined with the spherical harmonic

basis to represent view-dependent color. For each pixel on the camera plane, its color is calculated by blending N ordered 3D Gaussians above it:

$$C = \sum_{i \in N} c_i \alpha_i \prod_{j=1}^{i-1} (1 - \alpha_j), \quad (2)$$

where c_i , α_i are the color and opacity of the i -th Gaussian individual overlapping the current pixel. During the training of those Gaussians, they undergo alternant densification or sparsification according to the conditions of under- or over-reconstruction.

4 GaussianHead Method

Given a monocular video of the target person performing free head and facial movements, the corresponding expression parameters and masks of each frame, and known camera parameters, the proposed GaussianHead is trained on these four kinds of input. Our method models the complex head geometry based on anisotropic 3D Gaussians. Multi-resolution tri-plane with a learnable derivation strategy are leveraged to encode texture information for those Gaussian primitives. Using them, the final rendering with high fidelity is obtained. In inference, the approach can realize animation of the target subject by adjusting expression parameters and view directions. Fig. 3 illustrates the overall workflow.

4.1 Motion Deformation Field

The 3D Gaussian splatting technique was devised for the reconstruction of static scenes. However, human heads in our dynamic setting exhibit complex motions. To deal with this problem, a motion deformation field is constructed, the purpose of which is to obtain variable Gaussians connected with changing head motion attributes of the subject across different frames. Specifically, we first randomly initialize M Gaussians $\mathcal{G}_R = \{G(x_i, q_i, s_i)\}_{i=1}^M$, each of which is connected with three geometric variables: position x , rotation represented by unit quaternion q , and scaling vector s . Subse-

quently, we feed the pre-acquired facial expression representation e and the position x to a deformation network \mathcal{M}_d with a multi-layer perceptron (MLP) as its implementation. For a certain Gaussian, the deformation network predicts Δ_x , Δ_q , and Δ_s , which are offsets in terms of position, rotation, and scale:

$$(\Delta_x, \Delta_q, \Delta_s) = \mathcal{M}_d(\gamma(x), e), \quad (3)$$

where γ represents conducting position encoding on the mean position of the current 3D Gaussian, generating a high-dimensional sine-cosine sequence [Mildenhall *et al.*, 2021]. Next, we add the obtained offsets to their initial states, yielding \hat{x}_i , \hat{q}_i , and \hat{s}_i . Relevant updates are called core Gaussians $\mathcal{G}_C = \{G(\hat{x}_i, \hat{q}_i, \hat{s}_i)\}_{i=1}^M$ in the canonical space. For ease of expression, we denote the core Gaussian as G_C .

4.2 Learnable Gaussian Derivation

A single motion deformation MLP is sufficient to express complex head movements, but it struggles to simultaneously reconstruct all fine and intricate facial textures (see Sec. 5.5). To enhance the representation capability while using minor consumption, a multi-resolution tri-plane [Chan *et al.*, 2022] is employed to store texture information around the subject’s head. Let’s take the tri-plane at a specific resolution as an example. These factorized feature planes \mathbf{P}_{xy} , \mathbf{P}_{xz} , \mathbf{P}_{yz} have an identical size of (H, W, L) , where H and W represent the height and width and L denotes the channel length. Then, we derive K doppelgangers from each core Gaussian by imposing an equivalent number of learnable derivations parameterized by unit quaternion r on it. Note that K is required to evenly divide L . For every individual doppelganger, it is vertically projected onto three factor planes, generating three individual plane feature vectors by sequentially interpolating L/K channels of factor planes. Three shortened feature vectors from the tri-plane are fused by the Hadamard product, forming the sub-feature of the target doppelganger under the current resolution. We apply the same operations to this doppelganger at other resolutions and aggregate them through addition, generating the full feature vector of it with a size of L/K . Eventually, features from K doppelgangers are concatenated, yielding the canonical feature representation f for the core Gaussian. Mathematically, that can be expressed as

$$f = \bigcup_{i=1}^I \sum_{k=1}^K \prod_{j=1}^3 \varphi(\mathbf{P}_j, r_k(G_C)), \quad (4)$$

where I refers to the number of different resolutions considered for the tri-plane, and \mathbf{P} represents the parameterized plane with j indexing the xy , xz , and yz factorized planes. The symbol r denotes the derivation transformation, which is optimized also via a unit quaternion in our practice. In addition, φ indicates the projection of a doppelganger onto a factor plane and subsequent interpolation, and \bigcup means the feature concatenation.

The unit quaternions controlling the derivation do not have an explicit first-order gradient. Due to manifold constraints, they cannot be straightforwardly optimized in Euclidean space using first-order optimizers. Therefore, we employ the Riemannian ADAM optimizer [Béginneul and

Ganea, 2018], where updates to unit quaternions at the training step t are induced by an exponential term based on the learning rate α_t and gradient ∇_t in their tangent space:

$$r_{k,t+1} = r_{k,t} \text{Exp}(\alpha_t \nabla_t). \quad (5)$$

4.3 Hierarchical Radiance Decoding and Inherited Derivation Initialization

In contrast to recent dynamic scene approaches based on 3D Gaussians [Wu *et al.*, 2023; Yang *et al.*, 2023] that directly set opacity and color as optimizable parameters, we employ two small MLPs to decode the canonical features into opacity α and spherical harmonic coefficients Y_{lm} :

$$(\alpha, z) = \mathcal{D}_\alpha(f), \quad (6)$$

$$Y_{lm} = \mathcal{D}_c(d, z), \quad (7)$$

where z and d denote latent variables and view directions, and we use 4th-order spherical harmonic coefficients to synthesize view-dependent colors. This design ensures a more precise inference of texture (validated in Sec. 5.5). Finally, differentiable rasterization in Eq. 2 is used for rendering.

Recall that the number of Gaussian primitives dynamically increases or decreases during their training process. Given a new Gaussian copied by or split from the original entity, it proceeds to derive multiple doppelgangers (see Sec. 4.2) via optimizable rotations in our method. Regarding the optimization of rotation parameters, we employ an inheritance initialization strategy, which means initializing them with the same values used by the parent Gaussian. Experiments show that, compared to random or zero initialization, the inheritance strategy increases the training speed by approximately 14%. Relevant results are presented in the supplementary materials.

4.4 Training Objectives

We utilize L1 loss \mathcal{L}_{RGB} to measure the pixel-wise difference between the ground truth image and its corresponding rendering. The perceptual loss \mathcal{L}_{VGG} [Zhang *et al.*, 2018] and D-SSIM loss $\mathcal{L}_{\text{D-SSIM}}$ are leveraged to measure the quality loss of the rendered images. Specifically, for the perceptual loss, we use the first four layers of the VGG model [Simonyan and Zisserman, 2014] to extract feature maps from compared image pairs for subsequent similarity computation. The full objective function as well as its components are given as follows:

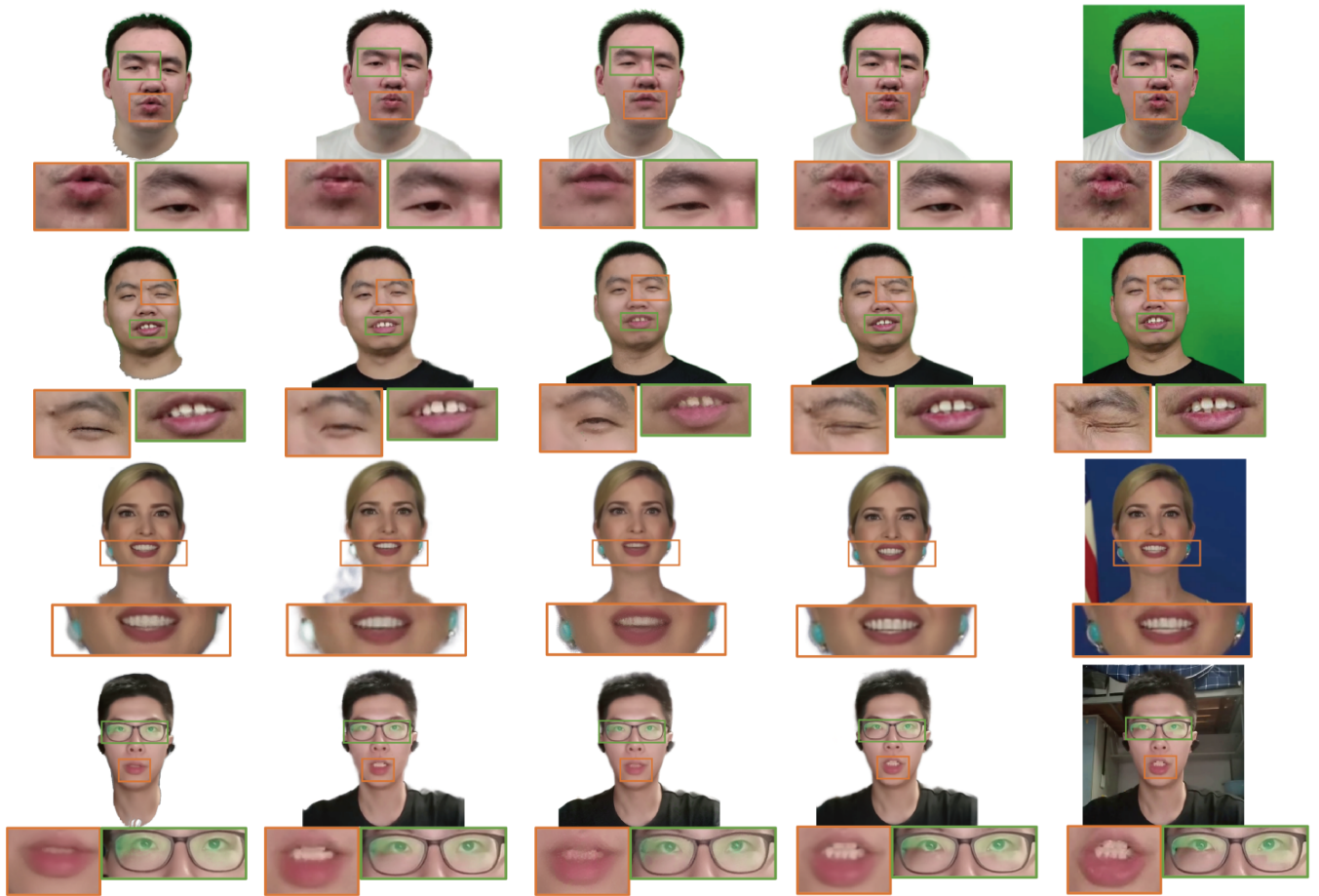
$$\mathcal{L} = \lambda_1 \mathcal{L}_{\text{RGB}} + \lambda_2 \mathcal{L}_{\text{VGG}} + \lambda_3 \mathcal{L}_{\text{D-SSIM}}, \quad (8)$$

$$\mathcal{L}_{\text{RGB}} = \|\mathbf{I} - \mathbf{I}^{\text{GT}}\|_1, \quad (9)$$

$$\mathcal{L}_{\text{VGG}} = \|\text{VGG}(\mathbf{I}) - \text{VGG}(\mathbf{I}^{\text{GT}})\|_1, \quad (10)$$

$$\mathcal{L}_{\text{D-SSIM}} = 1 - \text{SSIM}(\mathbf{I}, \mathbf{I}^{\text{GT}}), \quad (11)$$

where we empirically set $\lambda_1 = 0.8$, $\lambda_2 = 0.01$, and $\lambda_3 = 0.2$.



INSTA [Zielonka *et al.*, 2023] NeRFBlendShape [Gao *et al.*, 2022] PointAvatar [Zheng *et al.*, 2023]

Ours

GT

Figure 4: Qualitative comparisons between our GaussianHead and other approaches. All competitors were run under the configurations specified by their respective works. Our method achieves superior visual results, particularly in aspects such as wrinkles, teeth, eyebrows, and even reflections on glasses.

5 Experiments

5.1 Baselines

For comparison purposes, we chose state-of-the-art methods: INSTA [Zielonka *et al.*, 2023] based on volumetric NeRF, reconstructs avatars by building a neural surface on the foundation of 3DMM; PointAvatar [Zheng *et al.*, 2023] based on explicit points, constructs detailed avatars using iteratively refined and upsampled point clouds; NeRFBlendShape [Gao *et al.*, 2022] based on hybrid NeRF, utilizes a hash grid as the storage structure for the facial expression bases to construct head avatars.

5.2 Qualitative and Quantitative Comparison in Reconstruction

We showcase visual comparison results rendered by our method and baselines in Fig. 4. PointAvatar uses linear blend skinning (LBS) to control facial movements, which usually fail to fit extreme expressions. As evidence, please pay attention to the avatars generated by this approach in the 1st and 3rd rows, which show the actions of pouting and smile-

ing with squinted eyes, respectively. In addition, since the primitives adopted are points with fixed shapes, this approach may yield holes during reconstruction (please refer to more renderings from it in the appendix). NeRFBlendShape occasionally produces artifacts (see its rendering for the woman subject), which should be attributed to its adoption of a dynamic density grid update mechanism, leading to inaccurate density estimates of sampling points around the head space. INSTA models the head based on a predefined 3DMM geometry, making it struggle to represent the fine structures (such as the jewelry on the female in Fig. 4 and the suspended strands of hair in the appendix). Meanwhile, all of the above-compared methods come with a strong smoothing effect. In contrast, our GaussianHead can accurately render subtle details such as slightly closed eyes and wrinkles. Even if only a few frames show the oral cavity in the training data, we can achieve precise reconstruction (refer to Fig. 9). According to the best of our knowledge, this achievement is hard to obtain for previous head avatar approaches that also train their algorithms on monocular videos. The results of quantitative comparisons are reported in Table. 1. Under the L1, PSNR,

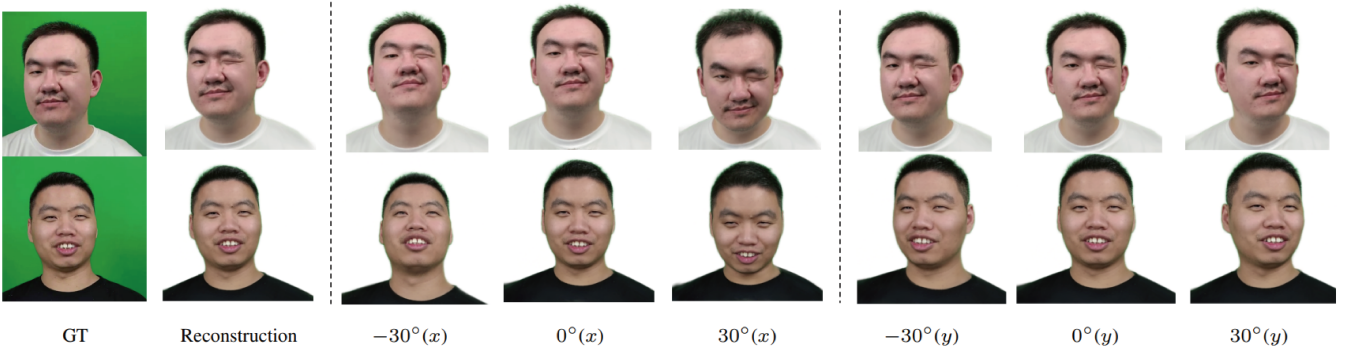


Figure 5: Novel view synthesis results of GaussianHead. We rotate the camera viewpoint around the x and y axes to acquire a novel view. From these new perspectives, there is a pronounced consistency in rendering details.

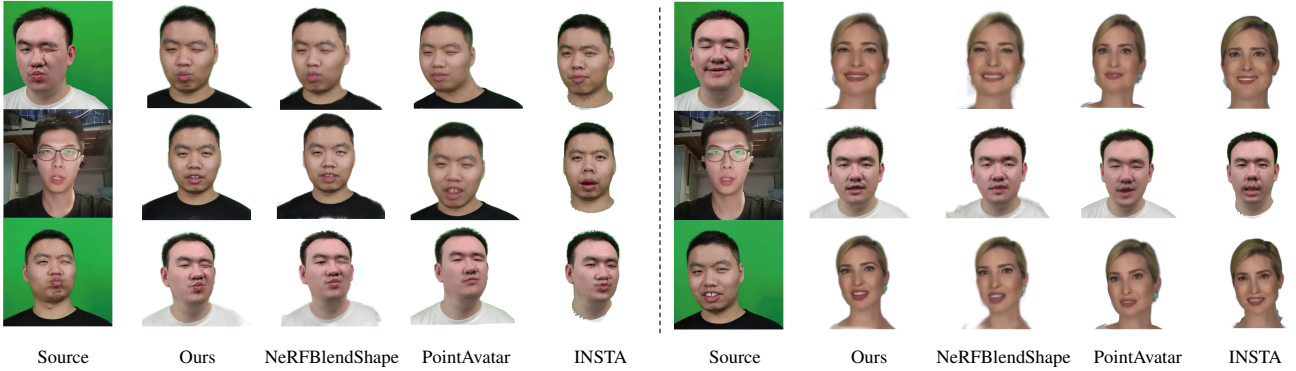


Figure 6: We use the source subject to drive the execution of new poses and expressions on reconstructed avatars. Our method achieves the best reenactment results, even in conveying extreme expressions.

Method	L1↓	PSNR↑	SSIM↑	LPIPS↓
INSTA [Zielonka <i>et al.</i> , 2023]	0.00182	27.41	0.892	0.141
NeRFBlendShape [Gao <i>et al.</i> , 2022]	0.00117	29.32	0.911	0.102
PointAvatar [Zheng <i>et al.</i> , 2023]	0.00211	26.76	0.861	0.162
GaussianHead (Ours)	0.00067	31.85	0.940	0.091

Table 1: In comparisons regarding the accuracy of reconstruction, our method achieved the best results.

SSIM and LPIPS metrics, we surpass the second best by a margin of 42.7%, 7.9%, 3.2% and 10.8%, respectively.

5.3 Novel View Synthesis and Cross-Identity Reenactment

The avatars generated by GaussianHead exhibit remarkable multi-view consistency, as illustrated in Fig. 5. The results show no artifacts or unrealistic facial expressions. At the same time, our method can also accurately represent details, such as teeth, from novel perspectives. Furthermore, we conducted a comparative study in the context of cross-identity reenactment with other methods. The head avatars obtained by GaussianHead excel at being precisely controlled by other characters. Our approach demonstrates outstanding performance in this task, particularly in the reenactment of extreme facial expressions. For example, the first and third rows on the left side of Fig. 6.

5.4 Different Number of Doppelgangers

The number of derived doppelgangers (K) significantly influences training time and the final rendering results. We conducted detailed experiments to determine the optimal value by setting it to five different values: 1, 2, 4, 8, and 16 (under the requirement that L is divisible by K). Additionally, we also investigated a dynamic K -scheduler for a more comprehensive evaluation: increasing K with the growing number of Gaussians:

$$K = \frac{L}{2^{t-u}}, u = \left\lceil \frac{n_i}{n_o} \right\rceil, \quad (12)$$

where L is the number of feature channels in each factor plane, n_i and n_o are the current and initialized number of Gaussians, $\lceil \cdot \rceil$ denotes the ceiling function, and t is a constant set to 6. Relevant experimental results are shown in Fig. 7. In the context of a fixed value, an excessively large K results in optimization challenges, notably evidenced by a pronounced deceleration in the optimization process at $K = 8$ and 16. Conversely, fewer doppelgangers were proven to be inadequate in addressing the issue of feature dilution, leading to a discernible deterioration in metrics. On the other hand, the incorporation of an adaptive changing scheme (i.e., K -scheduler) did not yield superior outcomes, which should be partially attributed to the predominant occurrence of newly introduced Gaussians in vacant regions. These regions, in

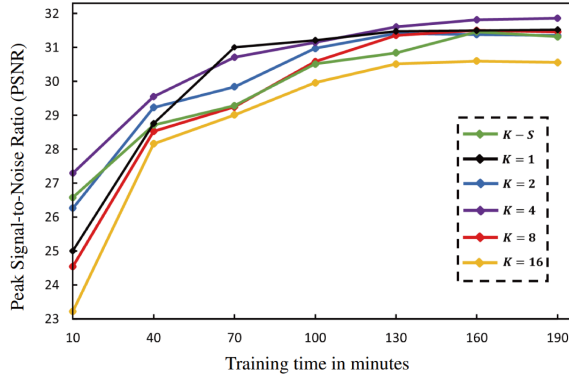


Figure 7: The performance of taking different values for K during the training process (“ $K-S$ ” represents the K -scheduler). Optimal performance is achieved when setting K to 4.

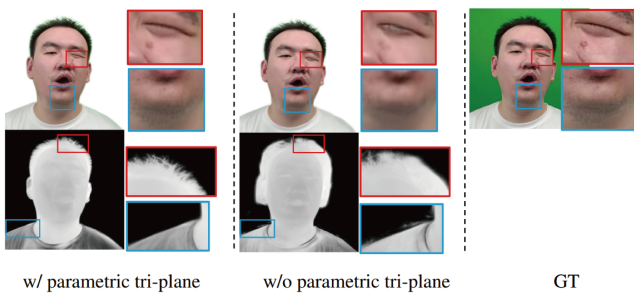


Figure 8: Visual comparisons of employing the parametric tri-plane structure to store Gaussians appearance information or not.

contrast to their densely optimized counterparts, have a low likelihood of feature dilution problems.

5.5 Ablation studies

Parametric tri-plane. We employ a parametric tri-plane as the container for Gaussian appearance information, where its planar grid encoding mechanism with multi-resolutions is beneficial to achieve high-detailed feature representation. For comparison, we ablate the parametric tri-plane, directly optimizing the opacity and spherical harmonic coefficients connected with 3D Gaussians. The ablation results given in Fig. 8 validate the effectiveness of our design. Simultaneously, the depth maps yielded by directly optimizing these two radiance parameters lead to numerous redundant Gaussians around the head that will not be removed because their opacity value is above the pre-defined threshold. This inevitably increases the overhead of training and causes negative perceptual impacts.

Learnable Gaussian Derivation. We conducted ablation experiments using axis-aligned mappings, like the practice conducted by the traditional tri-plane [Chan *et al.*, 2022; Fridovich-Keil *et al.*, 2023] (referred to as “w/o derivation” in Fig. 9 and Table. 2). Additionally, we also implemented a fixed set of rotations for the entire scene (called “global rotation”) like TILTED [Yi *et al.*, 2023], rather than individual primitives. The experimental results align with our analysis in Sec. 4.2, indicating the limitations of global rotation when applying it to complex dynamic scenarios.

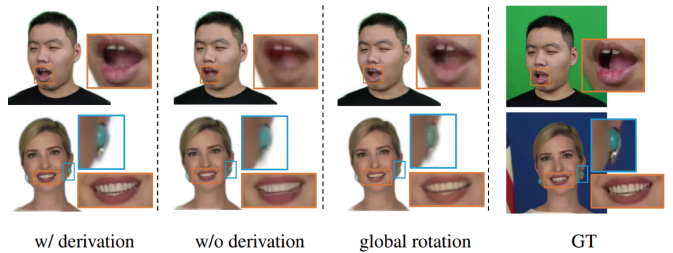


Figure 9: The novel Gaussian derivation strategy accurately restores features representing various complex structure regions, enabling the high-fidelity rendering of subtle details even for oral cavity rarely seen in the training data.

	L1↓	PSNR↑	SSIM↑	LPIPS↓
w/o Parametric Tri-plane	0.00090	30.47	0.891	0.144
w/o Derivation	0.00073	31.35	0.912	0.115
Global Rotation	0.00074	31.31	0.901	0.110
Ours Full	0.00067	31.85	0.940	0.091

Table 2: We systematically ablated several key components and assessed quantitative performance to demonstrate their effectiveness.

6 Limitation and Future Work

Although our method achieves excellent visual effects, it does not separate the motion of the head and torso, which may show unnatural shoulder shaking in rare scenarios where the head and torso have large motion differences (for a more intuitive demonstration, please refer to the video supplementary material). Existing separation methods either utilize semantic masks for independent training of the head and torso [Guo *et al.*, 2021; Tang *et al.*, 2022; Li *et al.*, 2023] or explicitly control their motion separately using the LBS algorithm of 3DMM [Zheng *et al.*, 2022; Zheng *et al.*, 2023]. The former complicates the entire training process and cannot achieve end-to-end training. The latter, although capable of separately controlling the broad-range pose movements of the head and torso, exhibits poor performance in controlling subtle expressions (because most complex expressions are challenging to articulate). Therefore, exploring a practical end-to-end method that achieves separate control of partial structures on the head while efficiently expressing subtle facial expressions is a promising avenue and a focus of our future work.

7 Conclusion

This paper introduces the GaussianHead based on 3D anisotropic Gaussians, which can construct high-fidelity head avatars and achieve reliable animations. Technically, we present an effective idea of applying Gaussian primitives to model geometrically variable heads in continuous motions and represent complex textures. Benefiting from multiple special designs, our method demonstrates remarkable performance even in rendering challenging cases, including skin details, fluffy hair, oral cavities with scarce training data, and extreme expressions. We believe that GaussianHead will provide universal inspiration for followers in this field.

8 Appendix

In the appendix, we first provided a detailed overview of our data acquisition method, training details, and network configuration. Following that, we showcased additional experimental results, including error maps and depth maps. Subsequently, experiments on determining the initialization scheme of derivation were presented.

A Implementation Details

A.1 Dataset Acquisition

To facilitate a fair comparison, all our data was sourced from public subjects [Gao *et al.*, 2022]. The training data for each subject comprised approximately 2000 to 2500 frames, and the test data was conducted using the last 3% to 5% of frames. Specifically, the data for each subject we used included only four parts: RGB head images with a resolution of 512×512 , expression parameters (derived from 3DMM model fitting [Gerig *et al.*, 2018]), camera parameters, and binary masks. The first three sections were all from open datasets, and the binary masks were created using MODNet [Ke *et al.*, 2022]. Our input frames employed binary masks to remove the background. In terms of head movement, we anchored the head in the coordinate system and simulated head pose changes using camera poses [Gafni *et al.*, 2021; Gao *et al.*, 2022].

A.2 Training Details

We implemented GaussianHead with PyTorch, where differentiable 3D Gaussian rasterization was implemented based on CUDA kernels [Kerbl *et al.*, 2023]. The initialization included 10K 3D Gaussians. Apart from optimizing the derivation quaternion using Riemannian ADAM [Bécinéul and Ganea, 2018], all other optimizers were first-order ADAM [Kingma and Ba, 2014]. Specifically, for the unit quaternion \mathbf{q} representing 3D Gaussian rotation, we followed the explicitly first-order gradients as derived in [Kerbl *et al.*, 2023] and also optimized it using ADAM. In our experiments, we set the batch size to 1 and trained on a single RTX 3090, taking approximately 3 hours. After 3000 iterations, we performed densification and pruning on 3D Gaussians every 500 iterations, pruning Gaussians larger than a certain proportion of the scene and removing Gaussians with opacity below the threshold. We set the size threshold for large Gaussians to be greater than 1% of the scene and the opacity threshold to 0.0002. Other details followed the settings in [Kerbl *et al.*, 2023].

A.3 Network Configuration

The network architecture is shown in Fig. 10. The main optimization parameters included the mean position \mathbf{x} , rotation \mathbf{q} , and scale \mathbf{s} of initial 3D Gaussians, as well as a motion deformation MLP, parameterized multi-resolution tri-plane, a radiance decoder MLP, and a set of learnable unit quaternions \mathbf{r} used for deriving each core Gaussian in canonical space. Positional encoding with a frequency of 10 was used for the initial Gaussians’ mean position \mathbf{x} in the input deformation network. The deformation network consisted of 8 linear layers with a width of 256, and skip connections were added in the

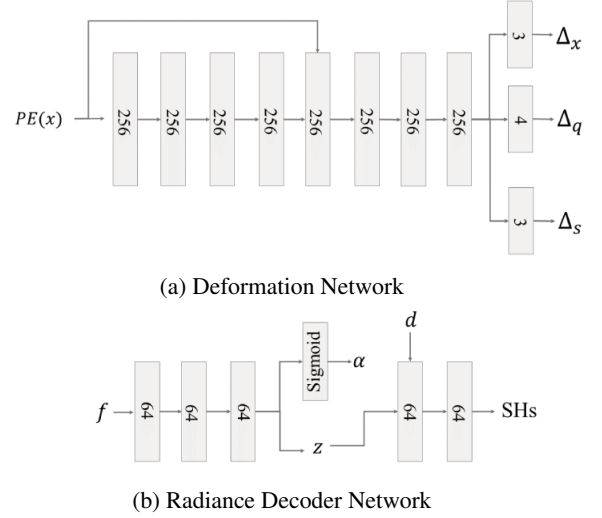


Figure 10: Our network architecture diagram provides a detailed overview of the network layers, width, and data flow. In subfigure a, $PE(\cdot)$ represents position encoding. Specific network parameter configurations are elaborated in Sec. A.3.

fourth layer. After the eighth linear layer, three output heads, respectively, outputted the position offsets $\Delta\mathbf{x}$, rotation offsets $\Delta\mathbf{q}$, and scale offsets $\Delta\mathbf{s}$ of the initial 3D Gaussians, all of which were activated using ReLU. The learning rate for the initial 3D Gaussian’s position was set to 1.6×10^{-4} , linearly decaying to 1.6×10^{-6} over training steps; rotation and scale had a learning rate of 1×10^{-3} . The initial learning rate for the motion deformation network was set to 8×10^{-4} , and it gradually decayed to 8×10^{-6} as the training progressed.

The parameters of the multi-resolution tri-plane were initialized with a uniform distribution in the range $[0.1, 0.5]$. The base resolution was set to 64×64 and multiplied by super-resolution scales: 1, 2, 4, and 8, resulting in the final four resolutions. For the canonical features, an opacity network with a width of 64 and 3 layers was used to process them. The opacity α was activated by the sigmoid, and the intermediate variables \mathbf{z} were concatenated with the view direction \mathbf{d} and fed into a color network with a depth of 2 and a width of 64. ReLU was used for activation to obtain spherical harmonic coefficients Y_{lm} . The learning rate for the parameterized tri-plane was 1×10^{-3} , linearly decaying to 0 at the last iteration; the learning rate for opacity was 1×10^{-4} . For learning the spherical harmonic coefficients representing view-dependent color, the learning rate for the first-order coefficient was 1×10^{-3} , and for the subsequent three-order coefficients, it was 5×10^{-5} .

A.4 Derivation Parameters Settings

Regarding the derivation unit quaternions \mathbf{r} , they were treated as trainable parameters, initialized with random numbers in the range $[0, 2^{32}]$, and uniformly distributed on a 3-dimensional hypersphere S^3 to obtain unit quaternions with better distribution properties. Their learning rate decayed from 1×10^{-3} to 0 at the last iteration.

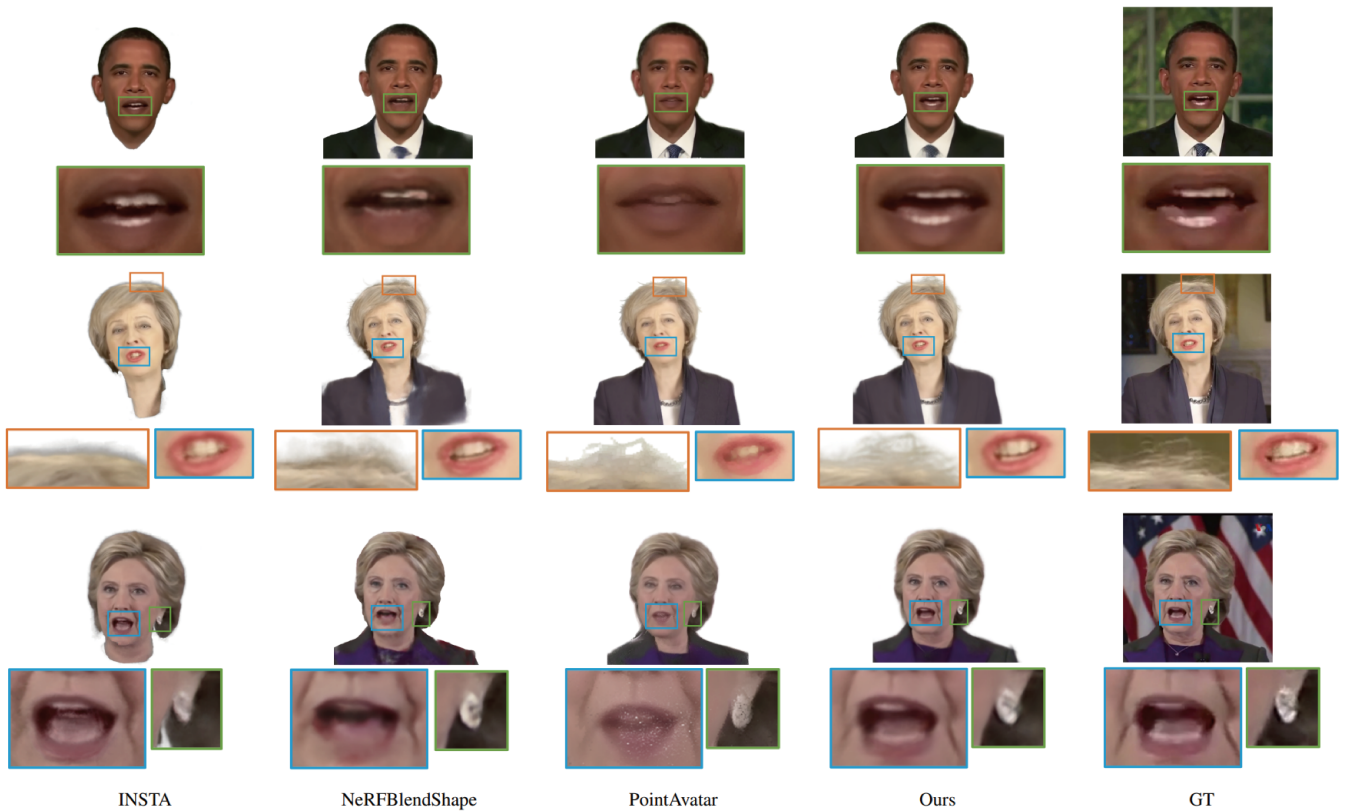


Figure 11: Comparison to other subjects, our approach continues to demonstrate better performance in both overall quality and finer details. For instance, it excels in capturing subtle elements such as individual strands of hair suspended above the head and intricate internal structures like the oral cavity.

	Inheritance Initialization	Random Initialization	Zero Initialization
Training Time (minutes)	180	210	208

Table 3: The optimization time required to achieve the optimal metrics regarding the initialization methods for three types of derived quaternions.

B More Results

B.1 Comparison of Other Subjects

We conducted experiments comparing other subjects, comparison methods include INSTA [Zielonka *et al.*, 2023], NeRFBlendShape [Gao *et al.*, 2022], and PointAvatar [Zheng *et al.*, 2023]. The experimental results are visible in Fig. 11.

B.2 Comparison of Error Maps

The error map, as opposed to the RGB image, can more clearly reflect the reconstruction accuracy. We calculated the L1 distance between the reconstructed images and ground truth on a per-pixel, and mapped it to the RGB space to generate the final error map, the results are presented in Fig. 12.

B.3 Accurate Depth Estimation

We additionally present the reconstructed precise depth maps in Fig. 13, from which it can be clearly seen whether there is

the presence of artifacts. Our method demonstrates excellent depth estimation performance.

C Parameter Experiments

C.1 Quaternion Initialization Method for Derivative

In the neural radiance field [Mildenhall *et al.*, 2021; Yi *et al.*, 2023], the number of sampled points in the scene is mostly fixed. However, our GaussianHead undergoes densification or pruning of 3D Gaussians as the iterations progress. For the 3D Gaussians that are clipped out, their quaternions used for controlling derivation were directly deleted. For the newly added 3D Gaussians that split from the parent Gaussian, three initialization schemes for derivation quaternions were evaluated: randomly initializing from the range $[0, 2^{32}]$ as done at the beginning of training, inheriting derivation parameters from the parent Gaussian, and zero initialization. The time required for these three approaches to achieve the optimal metrics of GaussianHead was compared in Tab. 3. Inheriting initialization helped avoid optimizing derivation parameters randomly or initializing them to zero from scratch, further reducing training time.

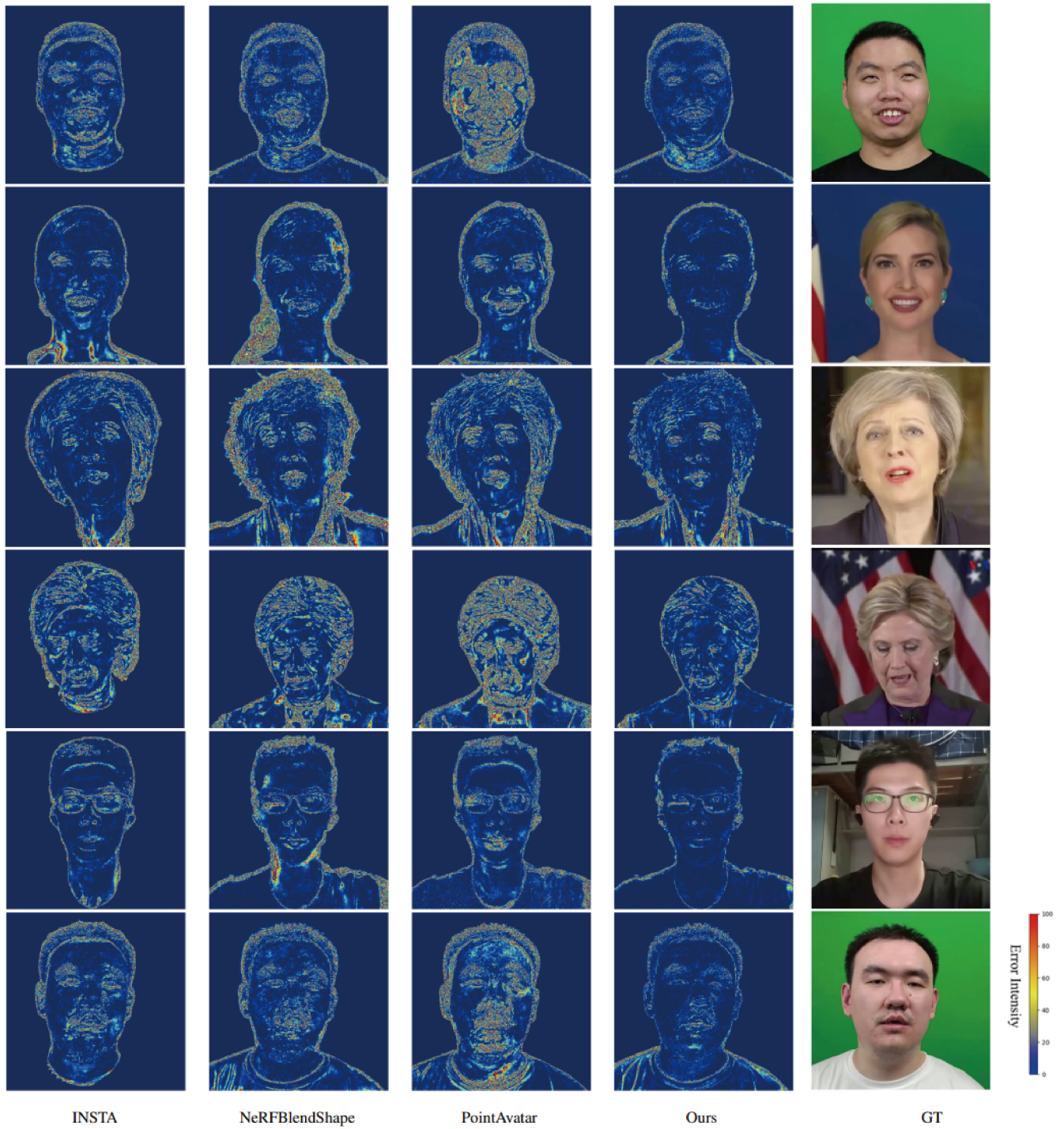


Figure 12: In comparison with INSTA, NeRFBlendShape, and PointAvatar on the error map, our approach exhibits the overall minimum reconstruction error, showcasing the highest quality of reconstruction.

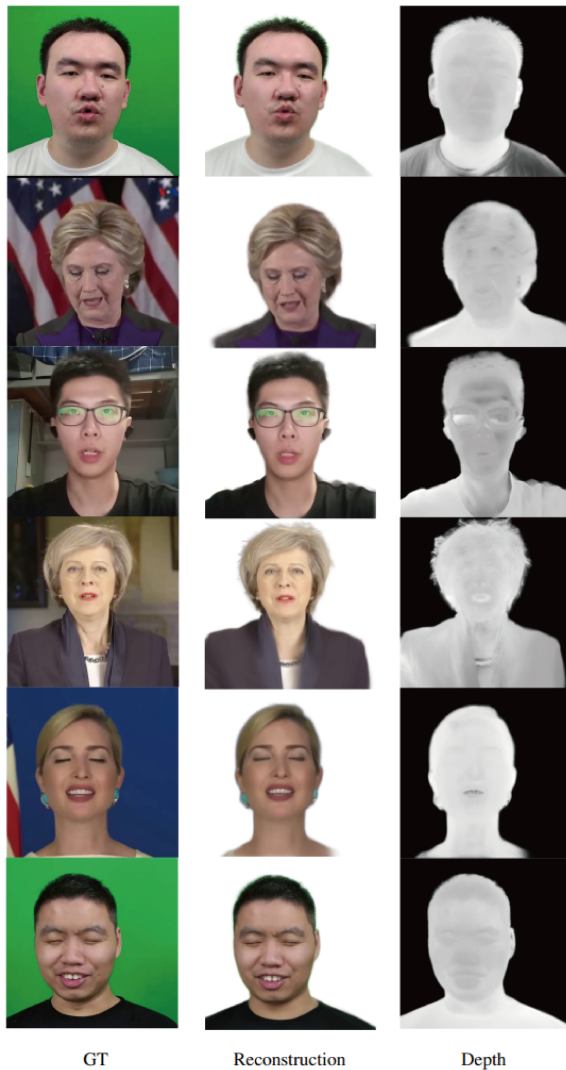


Figure 13: We reconstructed the ground truth image (left) into a head avatar (center) and simultaneously visualized the depth estimated by GaussianHead (right). Our method obtains accurate depth information.

References

- [Béginneul and Ganea, 2018] Gary Béginneul and Octavian-Eugen Ganea. Riemannian adaptive optimization methods. *arXiv preprint arXiv:1810.00760*, 2018.
- [Cao and Johnson, 2023] Ang Cao and Justin Johnson. Hex-plane: A fast representation for dynamic scenes. In *Proceedings of the IEEE/CVF Conference on Computer Vision and Pattern Recognition*, pages 130–141, 2023.
- [Cao et al., 2021] Chen Cao, Vasu Agrawal, Fernando De La Torre, Lele Chen, Jason Saragih, Tomas Simon, and Yaser Sheikh. Real-time 3d neural facial animation from binocular video. *ACM Transactions on Graphics (TOG)*, 40(4):1–17, 2021.
- [Chan et al., 2022] Eric R Chan, Connor Z Lin, Matthew A Chan, Koki Nagano, Boxiao Pan, Shalini De Mello, Orazio Gallo, Leonidas J Guibas, Jonathan Tremblay, Sameh Khamis, et al. Efficient geometry-aware 3d generative adversarial networks. In *Proceedings of the IEEE/CVF Conference on Computer Vision and Pattern Recognition*, pages 16123–16133, 2022.
- [Fridovich-Keil et al., 2023] Sara Fridovich-Keil, Giacomo Meanti, Frederik Rahbæk Warburg, Benjamin Recht, and Angjoo Kanazawa. K-planes: Explicit radiance fields in space, time, and appearance. In *Proceedings of the IEEE/CVF Conference on Computer Vision and Pattern Recognition*, pages 12479–12488, 2023.
- [Gafni et al., 2021] Guy Gafni, Justus Thies, Michael Zollhofer, and Matthias Nießner. Dynamic neural radiance fields for monocular 4d facial avatar reconstruction. In *Proceedings of the IEEE/CVF Conference on Computer Vision and Pattern Recognition*, pages 8649–8658, 2021.
- [Gao et al., 2022] Xuan Gao, Chenglai Zhong, Jun Xiang, Yang Hong, Yudong Guo, and Juyong Zhang. Reconstructing personalized semantic facial nerf models from monocular video. *ACM Transactions on Graphics (TOG)*, 41(6):1–12, 2022.
- [Gerig et al., 2018] Thomas Gerig, Andreas Morel-Forster, Clemens Blumer, Bernhard Egger, Marcel Luthi, Sandro Schönborn, and Thomas Vetter. Morphable face models—an open framework. In *2018 13th IEEE International Conference on Automatic Face & Gesture Recognition (FG 2018)*, pages 75–82. IEEE, 2018.
- [Guo et al., 2021] Yudong Guo, Keyu Chen, Sen Liang, Yongjin Liu, Hujun Bao, and Juyong Zhang. Ad-nerf: Audio driven neural radiance fields for talking head synthesis. In *IEEE/CVF International Conference on Computer Vision (ICCV)*, 2021.
- [Hong et al., 2022] Yang Hong, Bo Peng, Haiyao Xiao, Ligang Liu, and Juyong Zhang. Headnerf: A real-time nerf-based parametric head model. In *Proceedings of the IEEE/CVF Conference on Computer Vision and Pattern Recognition*, pages 20374–20384, 2022.
- [Ke et al., 2022] Zhanghan Ke, Jiayu Sun, Kaican Li, Qiong Yan, and Rynson WH Lau. Modnet: Real-time trimap-free portrait matting via objective decomposition. In *Proceedings of the AAAI Conference on Artificial Intelligence*, volume 36, pages 1140–1147, 2022.
- [Kerbl et al., 2023] Bernhard Kerbl, Georgios Kopanas, Thomas Leimkühler, and George Drettakis. 3d gaussian splatting for real-time radiance field rendering. *ACM Transactions on Graphics (ToG)*, 42(4):1–14, 2023.
- [Kingma and Ba, 2014] Diederik P Kingma and Jimmy Ba. Adam: A method for stochastic optimization. *arXiv preprint arXiv:1412.6980*, 2014.
- [Kirschstein et al., 2023] Tobias Kirschstein, Shenhan Qian, Simon Giebenhain, Tim Walter, and Matthias Nießner. Nersemble: Multi-view radiance field reconstruction of human heads. *arXiv preprint arXiv:2305.03027*, 2023.
- [Li et al., 2017] Tianye Li, Timo Bolkart, Michael J Black, Hao Li, and Javier Romero. Learning a model of facial

- shape and expression from 4d scans. *ACM Trans. Graph.*, 36(6):194–1, 2017.
- [Li *et al.*, 2023] Jiahe Li, Jiawei Zhang, Xiao Bai, Jun Zhou, and Lin Gu. Efficient region-aware neural radiance fields for high-fidelity talking portrait synthesis. In *Proceedings of the IEEE/CVF International Conference on Computer Vision*, pages 7568–7578, 2023.
- [Martin-Brualla *et al.*, 2021] Ricardo Martin-Brualla, Noha Radwan, Mehdi SM Sajjadi, Jonathan T Barron, Alexey Dosovitskiy, and Daniel Duckworth. Nerf in the wild: Neural radiance fields for unconstrained photo collections. In *Proceedings of the IEEE/CVF Conference on Computer Vision and Pattern Recognition*, pages 7210–7219, 2021.
- [Mescheder *et al.*, 2019] Lars Mescheder, Michael Oechsle, Michael Niemeyer, Sebastian Nowozin, and Andreas Geiger. Occupancy networks: Learning 3d reconstruction in function space. In *Proceedings of the IEEE/CVF conference on computer vision and pattern recognition*, pages 4460–4470, 2019.
- [Mildenhall *et al.*, 2021] Ben Mildenhall, Pratul P Srinivasan, Matthew Tancik, Jonathan T Barron, Ravi Ramamoorthi, and Ren Ng. Nerf: Representing scenes as neural radiance fields for view synthesis. *Communications of the ACM*, 65(1):99–106, 2021.
- [Müller *et al.*, 2022] Thomas Müller, Alex Evans, Christoph Schied, and Alexander Keller. Instant neural graphics primitives with a multiresolution hash encoding. *ACM Transactions on Graphics (ToG)*, 41(4):1–15, 2022.
- [Park *et al.*, 2019] Jeong Joon Park, Peter Florence, Julian Straub, Richard Newcombe, and Steven Lovegrove. Deepsdf: Learning continuous signed distance functions for shape representation. In *Proceedings of the IEEE/CVF conference on computer vision and pattern recognition*, pages 165–174, 2019.
- [Peng *et al.*, 2020] Songyou Peng, Michael Niemeyer, Lars Mescheder, Marc Pollefeys, and Andreas Geiger. Convolutional occupancy networks. In *Computer Vision—ECCV 2020: 16th European Conference, Glasgow, UK, August 23–28, 2020, Proceedings, Part III 16*, pages 523–540. Springer, 2020.
- [Simonyan and Zisserman, 2014] Karen Simonyan and Andrew Zisserman. Very deep convolutional networks for large-scale image recognition. *arXiv preprint arXiv:1409.1556*, 2014.
- [Tang *et al.*, 2022] Jiaxiang Tang, Kaisiyuan Wang, Hang Zhou, Xiaokang Chen, Dongliang He, Tianshu Hu, Jingtuo Liu, Gang Zeng, and Jingdong Wang. Real-time neural radiance talking portrait synthesis via audio-spatial decomposition. *arXiv preprint arXiv:2211.12368*, 2022.
- [Teotia *et al.*, 2023] Kartik Teotia, Xingang Pan, Hyeonwoo Kim, Pablo Garrido, Mohamed Elgharib, Christian Theobalt, et al. Hq3davatar: High quality controllable 3d head avatar. *arXiv preprint arXiv:2303.14471*, 2023.
- [Wu *et al.*, 2023] Guanjun Wu, Taoran Yi, Jiemin Fang, Lingxi Xie, Xiaopeng Zhang, Wei Wei, Wenyu Liu, Qi Tian, and Xinggang Wang. 4d gaussian splatting for real-time dynamic scene rendering. *arXiv preprint arXiv:2310.08528*, 2023.
- [Xu *et al.*, 2022] Qiangeng Xu, Zexiang Xu, Julien Philip, Sai Bi, Zhixin Shu, Kalyan Sunkavalli, and Ulrich Neumann. Point-nerf: Point-based neural radiance fields. In *Proceedings of the IEEE/CVF Conference on Computer Vision and Pattern Recognition*, pages 5438–5448, 2022.
- [Xu *et al.*, 2023a] Yuelang Xu, Lizhen Wang, Xiaochen Zhao, Hongwen Zhang, and Yebin Liu. Avatar-mav: Fast 3d head avatar reconstruction using motion-aware neural voxels. In *ACM SIGGRAPH 2023 Conference Proceedings*, pages 1–10, 2023.
- [Xu *et al.*, 2023b] Yuelang Xu, Hongwen Zhang, Lizhen Wang, Xiaochen Zhao, Han Huang, Guojun Qi, and Yebin Liu. Latentavatar: Learning latent expression code for expressive neural head avatar. *arXiv preprint arXiv:2305.01190*, 2023.
- [Yang *et al.*, 2023] Ziyi Yang, Xinyu Gao, Wen Zhou, Shao-hui Jiao, Yuqing Zhang, and Xiaogang Jin. Deformable 3d gaussians for high-fidelity monocular dynamic scene reconstruction. *arXiv preprint arXiv:2309.13101*, 2023.
- [Yariv *et al.*, 2020] Lior Yariv, Yoni Kasten, Dror Moran, Meirav Galun, Matan Atzmon, Basri Ronen, and Yaron Lipman. Multiview neural surface reconstruction by disentangling geometry and appearance. *Advances in Neural Information Processing Systems*, 33:2492–2502, 2020.
- [Yariv *et al.*, 2021] Lior Yariv, Jiatao Gu, Yoni Kasten, and Yaron Lipman. Volume rendering of neural implicit surfaces. *Advances in Neural Information Processing Systems*, 34:4805–4815, 2021.
- [Yariv *et al.*, 2023] Lior Yariv, Peter Hedman, Christian Reiser, Dor Verbin, Pratul P Srinivasan, Richard Szeliski, Jonathan T Barron, and Ben Mildenhall. Baked sdf: Meshing neural sdfs for real-time view synthesis. *arXiv preprint arXiv:2302.14859*, 2023.
- [Yi *et al.*, 2023] Brent Yi, Weijia Zeng, Sam Buchanan, and Yi Ma. Canonical factors for hybrid neural fields. In *Proceedings of the IEEE/CVF International Conference on Computer Vision*, pages 3414–3426, 2023.
- [Yu *et al.*, 2023] Wangbo Yu, Yanbo Fan, Yong Zhang, Xuan Wang, Fei Yin, Yunpeng Bai, Yan-Pei Cao, Ying Shan, Yang Wu, Zhongqian Sun, et al. Nofa: Nerf-based one-shot facial avatar reconstruction. In *ACM SIGGRAPH 2023 Conference Proceedings*, pages 1–12, 2023.
- [Zhang *et al.*, 2018] Richard Zhang, Phillip Isola, Alexei A Efros, Eli Shechtman, and Oliver Wang. The unreasonable effectiveness of deep features as a perceptual metric. In *Proceedings of the IEEE conference on computer vision and pattern recognition*, pages 586–595, 2018.
- [Zhang *et al.*, 2021] Zhenyu Zhang, Yanhao Ge, Renwang Chen, Ying Tai, Yan Yan, Jian Yang, Chengjie Wang, Jilin Li, and Feiyue Huang. Learning to aggregate and personalize 3d face from in-the-wild photo collection. In *Proceedings of the IEEE/CVF Conference on Computer Vision and Pattern Recognition*, pages 14214–14224, 2021.

- [Zhang *et al.*, 2023] Zhenyu Zhang, Renwang Chen, Weijian Cao, Ying Tai, and Chengjie Wang. Learning neural proto-face field for disentangled 3d face modeling in the wild. In *Proceedings of the IEEE/CVF Conference on Computer Vision and Pattern Recognition*, pages 382–393, 2023.
- [Zheng *et al.*, 2022] Yufeng Zheng, Victoria Fernández Abrevaya, Marcel C Bühler, Xu Chen, Michael J Black, and Otmar Hilliges. Im avatar: Implicit morphable head avatars from videos. In *Proceedings of the IEEE/CVF Conference on Computer Vision and Pattern Recognition*, pages 13545–13555, 2022.
- [Zheng *et al.*, 2023] Yufeng Zheng, Wang Yifan, Gordon Wetzstein, Michael J Black, and Otmar Hilliges. Pointavatar: Deformable point-based head avatars from videos. In *Proceedings of the IEEE/CVF Conference on Computer Vision and Pattern Recognition*, pages 21057–21067, 2023.
- [Zielonka *et al.*, 2023] Wojciech Zielonka, Timo Bolkart, and Justus Thies. Instant volumetric head avatars. In *Proceedings of the IEEE/CVF Conference on Computer Vision and Pattern Recognition*, pages 4574–4584, 2023.
- [Zwicker *et al.*, 2001] Matthias Zwicker, Hanspeter Pfister, Jeroen Van Baar, and Markus Gross. Surface splatting. In *Proceedings of the 28th annual conference on Computer graphics and interactive techniques*, pages 371–378, 2001.
- [Zwicker *et al.*, 2002] Matthias Zwicker, Hanspeter Pfister, Jeroen Van Baar, and Markus Gross. Ewa splatting. *IEEE Transactions on Visualization and Computer Graphics*, 8(3):223–238, 2002.

D Broader Impact

GaussianHead reconstructs highly realistic digital portraits from easily captured monocular videos, providing inspiration for future applications such as remote meetings and virtual reality. However, it can also be conveniently used to create and control digital avatars of others from online videos or laptop cameras, thereby posing risks of forgery and misuse. Unfortunately, we cannot control the specific applications of the technology. Therefore, we will release the source code and all modified datasets for reference in the development of anti-forgery techniques. Additionally, GaussianHead-generated digital portrait data can also be utilized as training images for anti-forgery models.